# Neutron-induced reactions contributing to the background in $\gamma$-ray astrophysics missions

R. Coszach,[1] P. Duhamel,[2] W. Galster,[1] P. Jean,[3] P. Leleux,[1] J.-P. Meulders,[1] J. Vanhorenbeeck,[2] G. Vedrenne,[3] and P. von Ballmoos[3]

[1]*Institut de Physique Nucléaire, Université Catholique de Louvain, B-1348 Louvain-la-Neuve, Belgium*

[2]*Institut d'Astronomie et d'Astrophysique, Université Libre de Bruxelles, B-1050 Bruxelles, Belgium*

[3]*Centre d'Etude Spatiale des Rayonnements, Université Paul Sabatier, F-31028 Toulouse, France*

(Received 29 November 1999; published 22 May 2000)

Nuclear reactions induced by neutrons lead to the delayed emission of $\gamma$ rays contributing to the instrumental background in $\gamma$-ray astrophysics missions in space. The cross sections for the reactions $^{27}$Al$(n,2p)^{26}$Na, $^{27}$Al$(n,\alpha)^{24}$Na, and $^{56}$Fe$(n,p)^{56}$Mn were measured up to a neutron energy of 50 or 65 MeV. A simple model was developed that allows one to extrapolate cross sections to higher energies. The magnitude of the instrumental background lines induced in the detectors of ESA's future INTEGRAL mission is deduced from our measurements.

PACS number(s): 25.40.−h, 07.87.+v

## I. INTRODUCTION

In the last two decades, $\gamma$-ray astronomy has grown to a mature field, extending our knowledge of the emitted spectrum by several orders of magnitude over the previously detected energy range. In particular, $\gamma$-ray lines have become a very important diagnostic tool for identification of isotopes in the stellar environment, e.g., in the ejecta of explosive events. INTEGRAL, the next $\gamma$-ray mission of ESA to be launched in 2001 [1], is expected to improve on the present observations and to search for new stellar $\gamma$-ray sources. SPI, the $\gamma$-spectrometer of INTEGRAL (Fig. 1), is a major instrument onboard [2]; it consists of a set of 19 hexagonal HPGe detectors in a planar configuration, the field of view (FOV) of which is defined by a hexagonal shield made of BGO scintillator blocks covering the sides and the bottom of the detector array. Imaging is performed by the coded aperture method using a hexagonal uniformly redundant array made of tungsten elements at 1.7 m above the detector plane. The BGO shield is active, which means that a signal in a detector in coincidence with a BGO signal will be vetoed. Therefore the BGO shield acts not only to define the FOV, but also to reduce the instrumental background.

The purpose of the present work is to improve the understanding of delayed background events in the $\gamma$-ray lines in SPI. This background has the following origin: cosmic rays interacting in the satellite structure or in the BGO shield produce neutrons [3] as shown in Fig. 2. These secondary particles interact in turn with matter close to the detectors; radioactive nuclei are produced that decay through $\gamma$-ray emission, mostly on a time scale longer than the veto signal triggered in the shield by the incident proton. The important point is that decay $\gamma$ rays can be of the same energy or an energy close to the $\gamma$ rays of astrophysical interest. The estimation of this additional background requires in a first step the measurement of the cross sections of key reactions, which is the subject of the present paper, and in a second step, a complete simulation of $\gamma$ emission from material inside the shielding, which is done for two cases here. This paper is organized as follows: in Sec. II, key reactions studied in the present work are identified; in Sec. III, the experimental method is described while experimental results and calculations are presented in Sec. IV. Consequences for the performance of SPI are contained in Sec. V.

## II. REACTIONS STUDIED

Three reactions were measured in the present work: (i) $^{27}$Al$(n,2p)^{26}$Na, (ii) $^{27}$Al$(n,\alpha)^{24}$Na, and (iii) $^{56}$Fe$(n,p)^{56}$Mn. The motivation for selection of these reactions is the following.

### A. $^{27}$Al$(n,2p)^{26}$Na reaction

$^{26}$Na has a half-life ($\tau_{1/2}$) of 1.07 s and decays to the first excited state of $^{26}$Mg ($E_x = 1.809$ MeV) with a branching ratio ($B$) of 99%. This reaction may thus be a main contributor to the background in the famous 1809 keV line from the decay of stellar $^{26}$Al ($\tau_{1/2} = 7.16 \times 10^5$ yr). The measurement of the spatial distribution of $^{26}$Al has been a major achievement of the Comptel mission [4]. A sizable amount

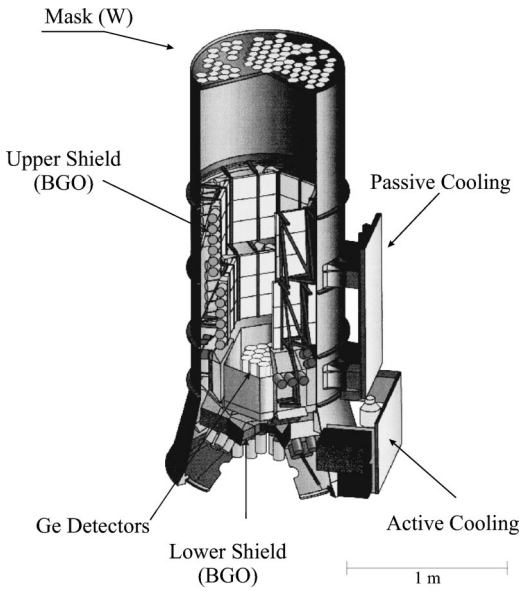


FIG. 1. Exploded view of SPI.

 

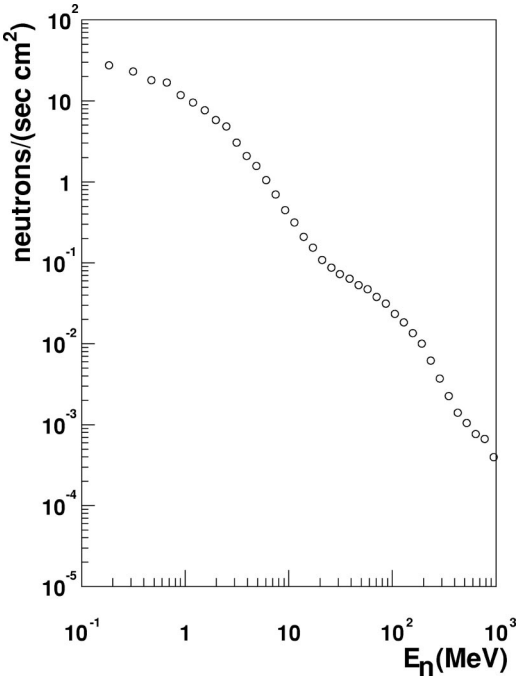


FIG. 2. Neutron energy distribution inside the SPI shield, as obtained in [3].

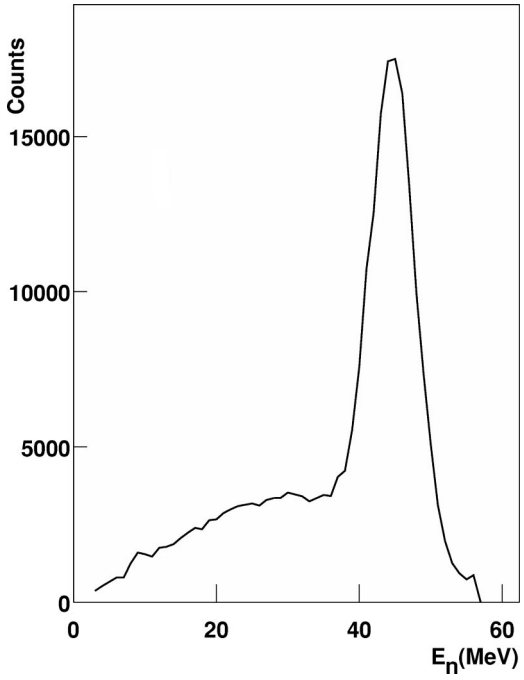


FIG. 3. Neutron energy spectrum resulting from the interaction of 48.5 MeV protons with a 5-mm-thick Li target. This energy spectrum is converted from a measured time-of-flight spectrum.

of $^{27}$Al is contained within the shielding of SPI, including capsules of the Ge detectors, for a total mass of 2700 g, in addition to the 91 kg of Al in the SPI structure. No data are available for this reaction.

### B. $^{27}$Al$(n,\alpha)^{24}$Na reaction

The interest in this reaction is to resolve the origin of an artifact which occurred during the Comptel mission: an excess of $\gamma$ rays in the 4–7 MeV energy range had been attributed to nuclear scattering ($^{12}$C or $^{16}$O on H) in the ORION region [5]; later on, however, it was realized that a summation of background $\gamma$ rays including the 1369 keV and 2768 keV lines from $^{24}$Na decays ($\tau_{1/2}=15$ h) produced by $^{27}$Al$(n,\alpha)$ could be in fact responsible for the observations [6]. Data exist for this reaction up to 20 MeV [7].

### C. $^{56}$Fe$(n,p)^{56}$Mn reaction

$^{56}$Mn ($\tau_{1/2}=2.6$ h) decays to several states in $^{56}$Fe including the first excited state ($E_x=847$ keV, $B=98.9\%$) which is a signature of the $^{56}$Ni$\rightarrow^{56}$Co$\rightarrow^{56}$Fe chain powering the light curve of supernovae [8]. Moreover, another line in $^{56}$Mn is at 1811 keV ($B=27\%$) and very close to the $^{26}$Al line, within the expected energy resolution of SPI (2 keV at 1 MeV). The quantity of iron within the SPI shield is 3170 g and the isotopic abundance of $^{56}$Fe is 91.7%. This reaction was previously measured up to a neutron energy of 20 MeV [9].

## III. EXPERIMENTAL SETUP

### A. Neutron beam

Neutrons are produced from the bombardment of a 5-mm-thick natural Li target by proton beams accelerated by the cyclotron CYCLONE in Louvain-la-Neuve. Beyond the target, protons are deflected downwards by a magnetic field and the beam current is integrated in a graphite Faraday cup. Neutrons are selected at 0° by a 2-m-long conical collimator, which defines a 3-cm-diameter spot at 330 cm from the target, where the samples are placed. The neutron spectrum consists of a high-energy peak from the unresolved $^7$Li$(p,n)^7$Be ground state (g.s.) and 0.47 MeV state, and a low-energy tail extending to threshold. In order to extract correctly the cross section at a given neutron energy one needs to know the distribution of the neutron energy at the sample position for each activation measurement. The neutron spectrum (Fig. 3) has been measured at three proton energies, 27, 48.5, and 63 MeV, by the time-of-flight method using a 3-cm-thick NE213 liquid scintillator of 5 cm diameter, whose efficiency above threshold was obtained from the SCINFUL code [10]. The NE213 detector was located at the place where samples were irradiated (see Sec. III B). The ratio of peak over continuum was determined and exhibits a dependence on the incident proton energy (81%, 65%, and 57% at 27, 48.5, and 62.9 MeV, respectively). The neutron spectra at other proton energies were then interpolated. The absolute number of neutrons was calculated from the target thickness, the integrated proton beam and the cross section of the high-energy peak [11]. The characteristics of the neutron beams, in particular the beam profile, have been studied extensively before [12]. It was shown that neutron collimation was very effective, and thus that the time-correlated background is strongly suppressed.

### B. Irradiation measurements

Samples were square plates of $50\times50$ mm$^2$ surface with 5 mm thickness for Al (99.999% purity) and 3 or 4 mm for

Fe. Each sample was placed in the neutron beam for a time adapted to the half-life of the product of interest, i.e., 1.07 s ($^{26}$Na), 2.6 h ($^{56}$Mn), 15 h ($^{24}$Na). For the latter two standard activation techniques were used, as samples could be irradiated for several hours ($\sim$8 h) before being removed from the beam and counted for several hours ($\sim$12 h) by a HPGe detector (90%) in a well-shielded place with a background of 7.5 counts/h in the 1.809 MeV $\pm$5 keV energy window. The first one, however, required a more sophisticated setup: the sample was irradiated for 3 s, moved downwards by 50 cm in 0.12 s in front of the Ge detector, and then counted for 9 s before being lifted back into the neutron beam. Movement of the sample was performed by a properly shaped cam connected to a motor with a moving time uncertainty of less than 1%. The Ge detector was well shielded by a heavy load of iron and it was not needed to lower the Ge voltage during irradiation periods. The beam was pulsed with a 3-s ON and a 9-s OFF period, and the measurement at a given energy lasted for several hours.

### C. Deduction of cross sections

In each irradiation, the cross section was obtained for a neutron energy domain corresponding to the high-energy peak in the spectrum. An algorithm had to be developed in order to subtract the contribution of the low-energy tail region. We started our measurements at a proton beam energy that provided a high-energy neutron peak as close as possible to the reaction threshold or to the highest-energy existing data. Thereafter, the proton beam energy was increased in steps of 8 MeV, corresponding to the full width of the high-energy neutron peak. In a particular irradiation, the measured number of $\gamma$ rays, $N_{\gamma tot}$, can be expressed as

$$N_{\gamma tot}=\sum_i N_{\gamma i}+N_{\gamma p},$$

where $N_{\gamma i}$ and $N_{\gamma p}$ are the number of $\gamma$ rays from bin $i$ of the continuum and from the peak, respectively; the number of $\gamma$ rays from the continuum is calculated from previous measurements at lower energy (either from this work or from other work). The cross section ($\sigma$) is related to the number of $\gamma$ rays by the expression

$$(nx)\sigma I=\frac{N_\gamma}{\epsilon},$$

where $I$ is the number of incident neutrons, $nx$ is the number of target atoms per cm$^2$ in the sample, and $\epsilon$ is the efficiency factor which will be described in the following.

The efficiency factor corrects for several effects.

(i) Time factors, i.e., irradiation time, transport time of the sample, and counting time were taken into account. Each was measured with an accuracy better than 1%.

(ii) Absolute detection efficiency of the HPGe detector; for counting, the sample was placed in contact with the entrance window of the 90% Ge detector. The GEANT code was used to take into account several effects: (a) the surface emitting $\gamma$ rays extends over a 30 mm diameter, and the neutron distribution over this surface is not uniform (the neutron beam has a halo [12]; (b) $\gamma$ rays are absorbed in the sample and in the front window of the detector; (c) $\gamma$ rays emitted in a cascade show an angular correlation which affects the summation effects. In our geometry, the effects related to cascade processes are not negligibly small: the detection efficiency of 1811 keV $\gamma$ rays in the full-energy peak drops from 4.6% to 3.3% when they are considered.

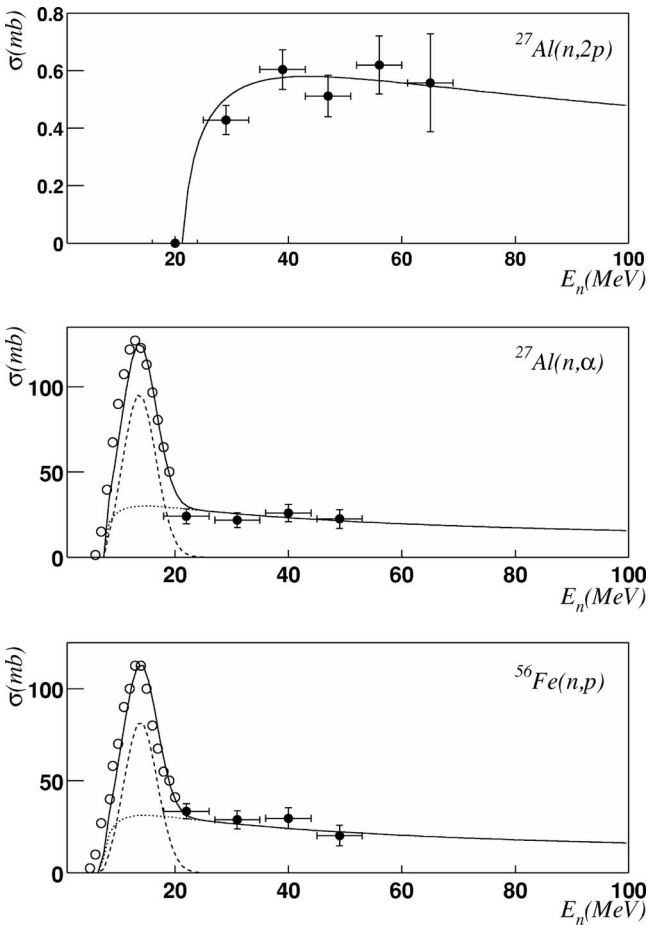


FIG. 4. From top to bottom: cross section for the $^{27}$Al$(n,2p)$, $^{27}$Al$(n,\alpha)$, and $^{56}$Fe$(n,p)$ reaction. Data from this work are solid circles. Data from previous work are open circles, and they are referenced to in Sec. II. The solid line is a global fit to the data: it is the sum of a direct component (dotted line) and a compound nucleus contribution (dashed line) (see Sec. IV).

The calculated efficiency factors were checked by measurements using an extended $^{22}$Na source, and by comparing experimental and computed spectra of the $^{56}$Fe$(n,p)$ reaction: in the latter, indeed, summation effects are important, as both the 1811 keV line and the 2113 keV line are emitted in a cascade with the 847 keV line. In all checks, measured and calculated efficiencies differed by less than 10%.

Cross sections are presented in Fig. 4. Horizontal bars span the full width of the high-energy peak; vertical bars contain the statistical error in the $\gamma$-ray peak integral and the systematic error in the efficiency factor $\epsilon$ added linearly. Additional systematic errors on the neutron flux (10%) and in the Li target thickness (5%) affect all data points but are not included in Fig. 4.

## IV. MODEL CALCULATIONS AND RESULTS

The purpose of this section is twofold. First, we devise a simple formalism for data fitting with a minimal number of free parameters allowing us to extract $\sigma(E)$, the energy dependence, from the data. Second, our aim is to obtain a global fitting to $\sigma(E)$ of different reaction data with a fixed set of parameters providing some predictive power in the absence of experimental evidence. A minimal model based on a semiclassical concept was developed to fit the data, which allows a reasonably accurate extrapolation of cross sections to higher incident neutron energies $E\sim 100$ MeV. It is thus possible to integrate the cross sections over the region of the main incident neutron flux from 1 to 100 MeV. We consider mainly two processes, the direct $(n,x)$ knock-out reaction (Sec. IV A) and the evaporation of particle $x$ from the compound nucleus following neutron induced fusion (Sec. IV B), where $x$ is a proton or $\alpha$ particle, respectively.

### A. Direct reaction

We calculate the phase space in the usual way for a Fermi gas in a spherical potential and obtain the energy density for spin 1/2 particles in the potential well:

$$\frac{dn}{dE}=\frac{2(m_0^{3/2}\tau)}{(\sqrt{2}\pi^2\hbar^3)}\sqrt{E-E_0}, \tag{1}$$

where $m_0$ is the nucleon mass, the volume of the potential well is $\tau=-V_0r^3$, and $E_0$ is the threshold energy of the $A(n,x)B$ reaction.

Using a volume integral per nucleon $\tau=377$ MeV fm$^3$, which includes the geometrical factor $4\pi/3$ for a spherical potential, one obtains

$$\frac{dn}{dE}=\frac{\sqrt{E-E_0}}{(5\sqrt{\mathrm{MeV}})}. \tag{2}$$

Note that the result is valid for a square well and for a Woods-Saxon form of volume $\tau$.

The transition probability is determined by Fermi's golden rule and the total direct $(n,p)$ or $(n,\alpha)$ cross section is thus assumed to have the form

$$\sigma_d(E)=(\pi\lambda\!\!\!^{-2})C_d(dn/dE), \tag{3}$$

and $C_d$ is a normalization variable.

In a direct $I(n,p)F$ or $I(n,\alpha)F$ reaction only a small fraction of the incident neutron energy is transferred into internal excitation energy of the residual nucleus $F$ and the transfer cross sections to individual levels are determined by nuclear structure. However, when averaged over many levels one expects that the sum of discrete cross sections can be described by an average behavior as is done in Eq. (3).

The cross section at energies close to the threshold, $E_0$, is influenced by the reaction $Q$ value, the Coulomb barrier for emitted charged particles, and the centrifugal barrier $V_l$ for $l>0$. One should thus replace $E-E_0$ in Eqs. (1) and (2) by $E+Q-V_c-V_l$. However, the transferred angular momenta in direct reactions being small, the centrifugal barriers can be neglected at incident energies well above the threshold. Furthermore, at low incident neutron energies $E<20$ MeV, the total $(n,p)$ and $(n,\alpha)$ yield contains a strong component from compound nucleus (CN) formation. The low-energy yield is in fact dominated by particle evaporation from the CN masking the effect of the centrifugal barriers in the threshold region for direct reactions. We can therefore neglect $V_l$ in this approach and simplify:

$$E_0=V_c-Q, \tag{4}$$

where $Q$ is the reaction $Q$ value and $V_c$ is the Coulomb barrier in the exit channel [see Eqs. 6(b),(c)].

After having fixed the potential volume at $\tau=377$ MeV fm$^3$, the only free parameter remaining is the normalization variable $C_d$. We obtain a good global fit to $(n,p)$ and $(n,\alpha)$ data from this work with $C_d=1.2$.

Al$(n,2p)$ data were well fitted with $C_d=(1.2/30)$ and $V_c=4.9$ MeV for successive $2p$ emission. It should be noted that the direct component in $(n,p)$ cross sections on heavier nuclei $(A>56)$ can be fitted as well with this model, provided $C_d$ is equal to $1.2\times 56/A$, where $A$ is the mass number of the target. Data obtained in our laboratory for the reaction $^{208}$Pb$(n,p)$ were fitted very satisfactorily this way [13].

### B. Evaporation from the compound nucleus

Below 20 MeV incident neutron energy, the $(n,p)$ and $(n,\alpha)$ yields are dominated by particle evaporation following fusion of the neutron with nucleus $I$. In contrast to the lack of data for direct $I(n,p)$ and $I(n,\alpha)$ reactions, a comprehensive compilation of activation data is available at low energies for $(n,p)$ and $(n,\alpha)$ cross sections. However, different data sets often disagree in absolute magnitude by a factor of 2, whereas the energy trends agree reasonably well with one another. Having obtained an expression for the direct part, we fitted the low-energy data $(E<20$ MeV) by adding a component due to evaporation of particle $x$ from the compound nucleus. Note that this is only possible because we can predict the direct part of $(n,x)$ from Sec. IV A in the energy range dominated by evaporation from the CN, as one cannot distinguish the two processes experimentally in an activation experiment.

We obtain a reasonably good fit to compiled data of $1p$ and $1\alpha$ evaporation by multiplying the expression in Eq. (3) by a Gaussian function and by replacing $C_d$ with a normalization variable $C_f$ for the fusion-evaporation part:

$$\sigma_{CN}(E)=(\pi\lambda\!\!\!^{-2})C_f(dn/dE)\exp\left(\frac{-(E-E_c)^2}{2s^2}\right) \tag{5}$$

with $s=3$ MeV, where the centroid $E_c$ in the Gaussian is adjusted to the data. A good approximation of the centroid from data fitting is obtained by

$$E_c=y9.5\ \mathrm{MeV}+V_c, \tag{6a}$$

where $y$ is the number of emitted nucleons. The Coulomb barrier for $I(n,x)F$ is evaluated as

$$V_c = \frac{e^2 Z_x Z_F}{r_0 (A_x^{1/3} + A_F^{1/3})},$$

with a relatively large value of $r_0$ due to the wave nature of light particles:

$$V_c = \frac{1.44 Z_F}{[1.7(1 + A_F^{1/3})]\ \text{MeV}} \tag{6b}$$

for $x = p$ and

$$V_c = \frac{2.88 Z_F}{[1.7(4^{1/3} + A_F^{1/3})]\ \text{MeV}} \tag{6c}$$

for $x = \alpha$, where $A_F$ and $Z_F$ are the mass and charge number of the final nucleus and $V_c$ is the Coulomb barrier of the evaporated particle $x$. In the case of multiparticle emission—e.g., $(n,2p)$—the Coulomb barrier is calculated for sequential emission of particles. Like $C_d$ in Eq. (3), $C_f$ is a dimensionless variable and good global fitting of the CN component is obtained by

$$C_f = 3.2. \tag{7}$$

The data and global fits to direct and CN components with $C_f = 3.2$ are displayed in Fig. 4, where the CN part was fitted with expressions (5)–(7). We did not aim at best fits with free parameters. Our main interest lies in obtaining a fair estimate of the overall behavior with one set of global parameters allowing us to predict the energy-integrated yields of $(n,p)$ and $(n,\alpha)$ reactions on the materials used in satellites and in satellite-based instrumentation, typically Be, Al, Fe, Cu. A reasonably precise estimate of the reaction rates for these stable nuclei is important, as such reactions might produce an intense radiation background. In this sense the obtained result is quite satisfactory.

We can summarize Eqs. (1)–(7) for $(n,x)$ yields as follows:

$$\sigma = \sigma_d + \sigma_{CN} = \pi \lambda\!\!\!^{-2} \frac{\sqrt{E + Q - V_c}}{(5\sqrt{\text{MeV}})} \cdots \times \left[ C_d + C_f \exp\left( \frac{-(E - 9.5 - V_c)^2}{18\ \text{MeV}^2} \right) \right], \tag{8}$$

where the cross section has the dimension $\text{fm}^2$, $E$, and $V_c$ are in MeV, and $C_d = 1.2$, $C_f = 3.2$.

### C. Low-energy resonances

In some cases, $(n,p)$ and $(n,\alpha)$ reactions on stable nuclei exhibit additional yields due to low-energy resonances, e.g., $^{32}$S and $^{58}$Ni in the low-energy domain, which are not accounted for in expression (8). Narrow resonances at low energy can be fitted with a Breit-Wigner term or by an $R$ matrix, which requires precise knowledge of resonance parameters. These contributions can be readily included but are not the subject of a minimal model intended to predict yields at higher energies. However, once the total width $\Gamma$ and level spacing $D$ reach a value $\Gamma/D \sim 1$, this resonant yield can be approximated by a cross section averaged over many resonances. One can expect that the energy dependence in the averaged resonant cross section results in a bell-shaped distribution of the cross section centered at the Coulomb barrier of the charged particle in the exit channel. In this case and when resonant yield data are available, the global fit at low energies can be improved considerably by adding a third term $\sigma_r$, like expression (5), where $E_c = 9.5\ \text{MeV} + V_c$ in (6a) is replaced by $E_c = V_c$ and $C_f \sim 3.2$ in Eq. (7) by $C_r \sim 12$, a normalization variable that is adjusted to the peak of the resonant yield:

$$\sigma_r = \pi \lambda\!\!\!^{-2} \frac{\sqrt{E + Q - V_c}}{(5\sqrt{\text{MeV}})} C_r \exp\left( \frac{-(E - V_c)^2}{18\ \text{MeV}^2} \right), \tag{9}$$

and $C_r \sim 12$.

TABLE I. Integral up to 100 MeV of the cross section for the $(n,p)$ reaction on Al, Fe, and Pb obtained from a global fit to the data, and ratio of the global fit to best fit of the same integrated cross sections.

| $A$ | Int. global fit (MeV b) | Ratio (global fit/best fit) |
|---|---|---|
| 27 | 2.598 | 0.978 |
| 56 | 2.567 | 0.966 |
| 208 | 0.704 | 1.176 |

### D. Integration of cross sections

A comparison of results obtained with the global parameters $C_d$, $C_f$ and best fits to the data with free parameters reveals that the total cross sections integrated up to 100 MeV differ by $<18\%$ between global and best fit (Table I). The difference between global and best fits is of the order of the absolute experimental errors and global fitting without free parameters appears to be sufficient.

Hence the minimal model is capable of providing a reasonably accurate albeit rough prediction of experimentally unknown $(n,p)$ and $(n,\alpha)$ cross sections in the energy range of 1–100 MeV for stable elements used in the construction of satellites and instrumentation. If $C_d$ and $C_f$ are treated as free parameters, more complex reactions such as $(n,px)$ can also be fitted successfully, e.g., $^{27}\text{Al}(n,2p)$ in Fig. 4. Expressions (8) and (9) can be readily energy integrated to obtain a prediction of the total yield or they can be input in analytical form into Monte Carlo simulations of precise configurations, allowing reliable estimates of the radiation background caused by incident cosmic rays. Needless to say, the minimal model approach can be applied to other cases [13] where total radiation yields must be estimated without reference to a well-established database.

## V. CONSEQUENCES FOR THE SPI PERFORMANCE

As mentioned in the Introduction, the measurement of cross sections is only the first step towards a precise deter-

mination of the neutron-induced background in SPI. The next step is a simulation of the delayed $\gamma$-ray emission from the activated isotopes in an exact mass model of SPI.

This simulation was performed for the case of $^{26}$Na produced by the $^{27}$Al$(n,2p)$ reaction. The neutron spectrum of Fig. 2 and the cross sections measured in this work and extrapolated up to 100 MeV by the model described in Sec. IV were used. As all Ge detectors are contained in Al capsules, we have in this case an important source of background (2.7 kg) very close to the detectors: the simulation resulted in a background in the 1809 keV line equal to $8\times10^{-3}$ counts per second. This number has to be compared to the signal expected from sources located in neighboring galaxies belonging to the local group. Estimations [14] yield a signal of $2\times10^{-6}$ $\gamma$-ray s$^{-1}$ cm$^{-2}$ from the closest galaxy, the Large Magellanic Cloud (LMC). The active surface of SPI is 263 cm$^2$, taking into account the part of the array in the shade of the mask, and the peak detection efficiency is 0.27 at 1809 keV. The signal from a source in LMC is thus $1.5\times10^{-4}$ s$^{-1}$, about 50 times smaller than the neutron-induced background. In practice, only $^{26}$Al from the Milky Way (expected intensity $4\times10^{-4}$ $\gamma$-ray s$^{-1}$ cm$^{-2}$) will thus be detected. The impact of the 1811 keV $\gamma$ ray from the $^{56}$Fe$(n,p)$ reaction on the 1809 keV $^{26}$Al line was not estimated here for several reasons: (i) it depends strongly on the energy resolution of the detectors; (ii) as the 1811 keV $\gamma$ ray is followed by a subsequent 847 keV $\gamma$ ray, a complete simulation including the angular correlation of both $\gamma$ rays is required: a background event will be effectively vetoed by a 847 keV $\gamma$ ray hitting the BGO shield.

As a second example, we refer to a reaction previously measured by our group, i.e., $^{9}$Be$(n,3n)^{7}$Be [15]. This reaction leads to the delayed emission of a 478 keV $\gamma$ ray; the expected observation of $^{7}$Be nuclei in the ejecta of novas is performed by analysis of the same line. Be is abundant inside the shield of SPI, as the cooling of the Ge array is obtained through thick Be plates (4.7 kg). A simulation of the induced background in the 478 keV line yields $6.4\times10^{-3}$ s$^{-1}$. This background is equal to the signal expected from a nova expelling $10^{-4}M_{\odot}$ at a distance of 1 kpc, immediately after outburst [16]. Only close novas can thus be detected.

It should be mentioned that the background and the signal in the $\gamma$-ray lines sit on top of a continuum that was not considered here. A correct estimation of the signal-to-background ratio will have to take this factor into account.

## VI. CONCLUSIONS

It is of primary importance to understand quantitatively the instrumental background of detectors used in space. It appears that secondary neutrons are major contributors to the background in the $\gamma$-ray lines of astrophysical interest, in particular the 1809 keV line of $^{26}$Al. In this work, the nuclear physics input to this problem was put on safer grounds: the cross section of three reactions was measured and a simple model was devised to reproduce the measured cross sections and to extrapolate them up to significantly higher energies.

## ACKNOWLEDGMENTS

We wish to thank the staff of the CYCLONE cyclotron for efficient run of the machine. The sample displacement in the measurement of the $^{27}$Al$(n,2p)$ reaction was realized by Ir. D. Breyne. This work was sponsored by the Interuniversity Institute for Nuclear Science, Brussels, and by a PRODEX grant from the Federal office for Scientific, Technical and Cultural Affairs, Brussels. P.L. is a Research Director of the National Fund for Scientific Research, Brussels.

[1] C. Winkler, in ''The Transparent Universe,'' Proceedings of the 2nd INTEGRAL Workshop, Report No. ESA SP-382 (1997), p. 573.
[2] P. Mandrou *et al.*, in ''The Transparent Universe'' [1], p. 591.
[3] P. Jean, Ph.D. thesis, University of Paul Sabatier, Toulouse, 1996.
[4] N. Prantzos and R. Diehl, Phys. Rep. **267**, 1 (1996).
[5] A. Bykov and H. Bloemen, Astron. Astrophys. **283**, L1 (1994).
[6] H. Bloemen *et al.*, in *The Extreme Universe*, Proceedings of the 3rd INTEGRAL Workshop [Astrophys. Lett. Commun. **38**, 349 (1999)].
[7] L.P. Geraldo, D.L. Smith, and J.W. Meadows, Ann. Nucl. Energy **18**, 293 (1989); Lu Han-Lin *et al.*, Nucl. Instrum. Methods Phys. Res. A **225**, 108 (1987).
[8] R. Diehl and F.X. Timmes, Publ. Astron. Soc. Pac. **110**, 637 (1998).
[9] M. Avrigeanu *et al.*, Z. Phys. A **329**, 177 (1988).
[10] J.K. Dickens, Report No. ORNL-6462, 1988.
[11] S. Schery *et al.*, Nucl. Instrum. Methods **147**, 399 (1977).
[12] C. Dupont *et al.*, Nucl. Instrum. Methods Phys. Res. A **256**, 197 (1987).
[13] R. Coszach *et al.*, Phys. Rev. C **61**, 054601 (2000).
[14] F.X. Timmes and S.E. Woosley, Astrophys. J. Lett. **481**, L81 (1997).
[15] P. Duhamel *et al.*, Nucl. Instrum. Methods Phys. Res. A **404**, 143 (1998).
[16] M. Hernanz *et al.*, Astrophys. J. Lett. **465**, L27 (1996).